Chapter 4

# Design, Power Electronics and Torque Control of Switched Reluctance Machines

Mircea Ruba and Petre Dorel Teodosescu

Additional information is available at the end of the chapter

http://dx.doi.org/10.5772/intechopen.69270

**Abstract**

In the last decade, increased tendency in the field of automotive industry was focused on the development of highly efficient and low-cost electric propulsion systems to replace the existing internal combustion solutions. The aim is to reduce the pollution due to carbon dioxide emissions into the air. Several electric machine topologies with their power electronics, control and supply units are continuously in the development process to reach the desired goal. One such machine is the switched reluctance machine (SRM), reaching increased power density, low cost and possibility of continuous operation despite fault occurrence. Designing the machine, choosing its power electronics and controlling the machine to diminish the negative effect of the torque ripples are key points in reaching the proper propulsion system. The main topics presented in detail in this chapter are managing the reader's skills with an analytic design breviary, presenting the machine's control strategies for instantaneous torque linearization and finally, showing a power converter topology with increased performances in low voltage applications. To be more close to such an application, the exampled machine is developed for a light electric vehicle for people with physical disabilities. Operational skills of the machine will be validated based on complex simulations.

**Keywords:** switched reluctance machine (SRM), design breviary, power electronics, torque smoothening, light electric vehicle

## 1. Introduction

Nowadays, research activity in the field of automotive industry receives a strong influence due to necessity to reduce the emissions of polluting gasses in the atmosphere. Hence, replacing the classical internal combustion engines with electric propulsion systems that are non-polluting

became a hot topic in research labs all over the world [1]. Different electrical machine structures, their power electronics and supply units are continuously developed and tested, aiming the goal of high efficiency at as low costs as possible. Induction machines and permanent magnet machines are now implemented on Tesla and Toyota electric vehicles. However, their design and building costs are higher compared with other machine topologies, such as the switched reluctance machine (SRM). The latter has the main drawback of more complex power electronics and complex control. However, with the advance of the semiconductors and processors, it became possible to develop reduced price electronics and their applied control for SRMs.

Another feature of the SRM is the ability to continuously operate even in faulted conditions and if added to the original topology, structural modifications one can reach a highly fault tolerant propulsion machine [2].

Designing an SR machine is not too complicated, however, it is important to establish during sizing process, proper flux density values in the magnetic core. Too low values have the outcome of an unsaturated machine and by this, poor power density and too high values will limit the developed power and cause core heating [3]. Proper sizing of the air-gap is having huge performance influence; hence, a compromise must be considered between low values and building costs that are increasing drastically for values smaller than 0.5 mm.

Choosing and designing the proper architecture for the power electronics for an SR machine is crucial from the point of view regarding costs and ability to perform torque linearization control. If no such dedicated control is required, only classical hysteresis one is engaged, there are simple power converters that can be used with minimal number of transistors. However, if one desires to develop and use torque smoothening procedures, topologies that allow these are mandatory to be used, based on complete or half-H bridge designs, with independent switch control. Moreover, the driver that turns on/off the power switches must be able to maintain the state of the switch for an unlimited time [4].

A serious drawback of the SRM is the increased torque ripples that are caused due to the working principle of the machine to switch the current from one phase to the next one that encounters the lowest magnetic reluctance. By this, the rotor moves from unaligned to aligned rotor to stator poles, the movement being characterized by a sudden instantaneous torque variation. Part of the torque ripple minimization can be handled during the design phase [5], shaping correctly the rotor poles function of the stator ones. However, this is limited up to an extent that is still considered too much for automotive applications. The main method for decreasing as much as possible the torque ripples that create mechanical stress, noise and vibrations is to engage direct instantaneous torque control (DITC) of current profiling based on torque sharing functions (TSF). For both, as mentioned in the previous paragraph, it is necessary to have certain electronics that allow their operation. Following the details presented in this chapter, one can see that the toque characteristic of the SRM can reach a shape just like that of an induction or synchronous motor, yet using a much cheaper and more simple machine structure.

To be more comprehensive when designing such a machine, it is more transparent if one considers a specific application. For this case, the application will be a light electric vehicle designed for people with physical disabilities. Based on an existing DC machine mounted on

such a vehicle, the main parameters that will be the start-up for the design process are: the required output power ($P_{2N}$) 1.2 kW, the supply voltage ($U_N$) of 24 V, shaft speed ($n_N$) of 3400 rpm and electromagnetic required torque ($T$) of 3.4 Nm. Besides these considerations, it is mandatory that the machine needs to fit in the place of the existing DC machine. Hence, the maximum dimensions allowed are as follows: for the outer diameter 115 mm and for the active stack length 150 mm.

## 2. Design of the switched reluctance machine

Based on the specifications detailed in the introduction part, one can start sizing the SRM. Before that the stator ($Q_S$) and rotor ($Q_R$) pole numbers must be imposed. Usually, three-phase SRMs are cheaper both in electronics and machine building, but encounter high torque ripples, while five- or six-phase machine with low torque ripples reach increased development costs. Hence, the best compromise is to develop a four-phase machine, with a $Q_S/Q_R$ ratio of 8/6 [6]. Another parameter that must be imposed is the flux density toward the air-gap ($B_{gmax}$) at 1.9 T. The current computed function of the supply voltage and the machine's requested power, considering an efficiency of 0.65 (low power SRMs have quite poor efficiency) is $I$ = 80 A. The design process is an iterative one, as this will be explained later. Hence, the air-gap was set to a low value of $g$ = 0.1 mm, this is due to the dimension limitations of the outer machine diameter.

The most influential parameter of the machine is the mean diameter [7] ($D_g$).

$$D_g = \sqrt[3]{\frac{P_{2N} \cdot Q_s \cdot k_\sigma}{Q_R \cdot \pi^2 \cdot k_L \cdot \frac{n_N}{60} \cdot B_{gmax} \cdot \left(1 - \frac{1}{K_{cr}}\right) \cdot A_S}} \tag{1}$$

In Eq. (1), $k_\sigma$ and $k_L$ coefficients are the leakage flux factors, chosen between 0.75 and 0.95, respectively, the aspect factor, which can be calculated from the rotor pole number using Eq. (2).

$$k_L = \frac{\pi}{2} \cdot \frac{1}{\sqrt[3]{Q_R}} \tag{2}$$

It should be mentioned that for this particular design, as the active stack length is given in the specifications, one does not need to compute it any more. The term $A_s$ represents the electrical loading that is chosen in the range 25,000–100,000 A/m, where higher values correspond to smaller dimensions [8]. Carter's factor ($K_{CR}$) considers the flux path's distortion due to the shape of the salient poles. Its value ranges between 1.4 and 2. The ratio of the mean diameter with respect to the aspect factor will give an estimate of the active stack length of the machine ($l_S$), but as mentioned for this design, this is a known value.

The stator and rotor pole pitch is computed as ratio between the mean diameter and the number of the poles, using Eq. (3).

$$\tau_{S,R} = \pi \cdot \frac{D_g}{Q_{S,R}} \tag{3}$$

The width of the stator and rotor poles ($b_{pS}$ and $b_{pR}$) can be calculated by using the pole pitch values, considered about 0.1–1.3 of it. The values chosen for stator and rotor were, respectively, 0.8 and 1.15 to reach as low torque ripples as possible [6]. Using these values, the yokes of the stator and rotor can be computed considered in the range of 0.5–1 of the pole width. Smaller values will reach proper saturation in the magnetic cores [5, 9] which will help to extract the energy from the coils when the phase is turned off. However, too low values will saturate the core too much resulting in the overheating of machine.

The slot openings are used to determine function of the stator and rotor pole widths and the pole pitch values computed with Eq. (3).

$$b_{cS,cR} = \tau_{S,R} - b_{pS,pR} \tag{4}$$

Using a catalogue value for the shaft ($d_{ax}$) one can now finalize the sizing process that regards the SRM's rotor. The rotor pole height, meaning the dimension from the airgap to the rotor yoke, and the inner rotor diameter will be computed using Eqs. (5) and (6), both function of the rotor yoke height ($h_{jR}$).

$$h_{pR} = \frac{D_g - g}{2} - h_{jR} - \frac{d_{ax}}{2} \tag{5}$$

$$D_{iR} = D_g - g - h_{jR} - h_{pR} \tag{6}$$

To finalize the sizing process with regard to the stator; firstly, it is necessary to size the coils of the machine, because these influence the height of the stator poles. This process starts from the magnetomotive force (mmf). There are several methods to compute it, but one efficient and simple way is to take advantage of the known parameters, such as the air-gap length ($g$) and its flux density value ($B_{gmax}$), the saturation factor, the flux leakage factor ($k_\rho$) and the relative permeability of the air ($\mu_0$).

$$\Theta = \frac{g \cdot k_{sat} \cdot B_{gmax}}{k_\rho \cdot \mu_0} \tag{7}$$

Now a round value of the number of turns can be established as a function of the magnetomotive force and the phase current ($I$) of the SRM.

$$N_f = \text{round}\left(\frac{\Theta}{I}\right) \tag{8}$$

Next, sizing the cross-section of the wire has handled function of the current density ($J_c$) in the range of 2.5–8 A/cm$^2$.

$$S_{cond} = \frac{I_{rms}}{J_c} \tag{9}$$

In Eq. (9), it is seen the rms value of the current ($I_{rms}$) is used instead of its rated value. The reason is that the current is switched from one phase to another, and the machine has four phases; one phase will be energized for only ¼ of the entire period. Hence, the rms current will be computed as the function of the number of phases ($N_{phase}$) like in AC supply systems, based on Eq. (10).

$$I_{rms} = \frac{I}{\sqrt{N_{phase}}} \tag{10}$$

The used wire diameter can be computed as the function of the cross-section in Eq. (9). This value will be used for arranging the turns inside the stator slots, as it will be presented as follows. The total number of turns is placed in several layers. Each layer will have a certain number of turns ($N_{sp\_strat}$), computed function of the slot opening ($b_{cS}$), its insulation ($g_{iz}$) and the actual wire diameter.

$$N_{sp\_strat} = \text{round}\left(\frac{l_{bob} - 2 \cdot g_{iz}}{1.05 \cdot d}\right) \tag{11}$$

The number of layers ($n_{strat}$) is found by dividing the total number of turns by the number of turns in a layer. Now, the height of the coil can be used to find the function of the number of layers, the wire diameter and the isolation of each wire ($g_{iz\_strat}$), using Eq. (12).

$$h_{bob} = n_{strat} \cdot (d + g_{iz\_strat}) + 2 \cdot g_{iz} \tag{12}$$

The area inside the stator slot occupied by the coil is used to compute function of the number of turns, the cross-section of the wire and a factor ($k_u$) ranged between 0.5 and 0.85 that considers the wire surface imperfections.

$$A_{bob} = N_f \cdot \frac{S_{cond}}{k_u} \tag{13}$$

The term $A_{bob}$ is used for only half of the stator slot. In one slot, two such areas need to fit as two phases sharing the same slot. Hence, the total slot area will be computed using Eq. (14).

$$A_c = 1.1 \cdot 2 \cdot A_{bob} \tag{14}$$

The term '1.1' is added as a safety caution because there are other imperfections of the coils that cannot be taken into calculation every time. Having these dimensions fixed, one can compute the height of the coil using Eq. (15).

$$h_{cS} = \text{round}\left(\frac{A_c}{b_{cS}}\right) \tag{15}$$

Usually for simplifying the cutting process, round values are imposed. At this point, it is easy to find the height of the stator pole ($h_{pS}$), adding to the height of the coil the height of a nonmagnetic displacer ($h_{lim}$) used to fix the coil into the slot.

$$h_{pS} = h_{cS} + h_{lim} \tag{16}$$

At this point, having all the required dimensions, it is possible to compute the outer diameter of the machine, for this project, to check if this does not exceed the imposed value.

$$D_M = D_g + g + 2 \cdot h_{pS} + 2 \cdot h_{jS} \tag{17}$$

To be able to compute the resistance of one phase winding, it is necessary to know the wire length function of the machine dimensions.

$$l_{inf} = 2 \cdot N_f \cdot (l_S + h_{jS}) \tag{18}$$

Finally, the resistance is given by Eq. (19) considering the cross-section and the material properties.

$$R = \rho_{Cu} \cdot \frac{l_{inf}}{S_{cond}} \tag{19}$$

### 2.1. Analytic calculation of losses and torque in SR machines

To calculate the efficiency of the newly designed SR machine, different methods for losses approximation can be used [7, 10]. Preliminary, it is mandatory to compute the frequency of the flux density variation in the magnetic core, both for the stator and the rotor.

$$\begin{aligned} f_{jS} &= \frac{Q_S}{2} \cdot \frac{n_N}{60} \\ f_{jR} &= \frac{Q_R}{2} \cdot \frac{n_N}{60} \end{aligned} \tag{20}$$

The specific losses in the machine's core, computed for standard values measured for 50 Hz and 1 T are calculated using Eq. (21), where $B_{jS}$ and $B_{jR}$ are the stator and rotor yoke flux densities.

$$\begin{aligned} p_{FeS} &= p_{Fesp} \cdot B_{jS} \cdot f_{jS} \\ p_{FeR} &= p_{Fesp} \cdot B_{jR} \cdot f_{jR} \end{aligned} \tag{21}$$

To calculate the losses in the machine and function of its dimensions, one needs to compute the weight of the assemblies of the core function of the used material's properties.

$$\begin{aligned} G_{FejS} &= \pi \cdot \left[ \frac{D_M^2}{4} - \left( \frac{D_M}{2} - h_{jS}^2 \right)^2 \right] \cdot l_S \cdot \rho_{Fe} \\ G_{FejR} &= \pi \cdot \left[ \left( h_{jR} + \tfrac{d_{ax}}{2} \right)^2 - \left( \tfrac{d_{ax}}{2} \right)^2 \right] \cdot l_S \cdot \rho_{Fe} \\ G_{FepS} &= Q_S \cdot b_{pS} \cdot h_{pS} \cdot l_S \cdot \rho_{Fe} \\ G_{FepR} &= Q_R \cdot b_{pR} \cdot h_{pR} \cdot l_S \cdot \rho_{Fe} \end{aligned} \tag{22}$$

The losses in the winding have computed function of the internal resistance and the phase current.

$$P_{\mathrm{j}} = R \cdot I^2 \tag{23}$$

The mechanical losses are estimated approximately 0.5% of the machine's output power.

$$P_{\mathrm{M}} = 0.005 \cdot P_{2\mathrm{N}} \tag{24}$$

Finally, the total losses of the machine will be the sum of the above calculated ones:

$$P_{\mathrm{T}} = P_{\mathrm{j}} + P_{\mathrm{Fe}} + P_{\mathrm{M}} \tag{25}$$

Hence the efficiency will be

$$\eta_{\mathrm{SRM}} = \frac{P_{\mathrm{out}}}{P_{\mathrm{out}} + P_{\mathrm{T}}} \tag{26}$$

The developed torque can be used to compute function of the mmf created in the machine and its main dimensions using Eq. (29).

$$T_{\mathrm{SRM}} = 2 \cdot (N_{\mathrm{f}} \cdot I^2) \cdot \frac{D_{\mathrm{g}}}{2} \cdot \mu_0 \cdot \frac{l_{\mathrm{S}}}{2g} \tag{27}$$

The term $2g$ (twice the air-gap) in Eq. (29) stands because always two diametrically opposed poles contribute to the torque development, hence, the air-gap length is considered double along the flux path.

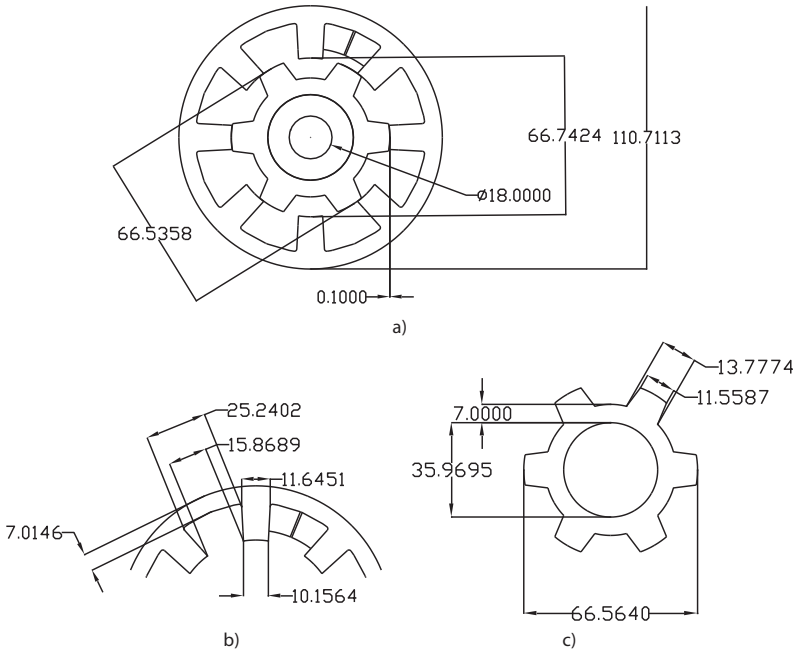


**Figure 1.** The resulted SRM dimensions: (a) the entire machine, (b) details of the stator and (c) details of the rotor.

Starting from the requirements detailed at the beginning of the chapter and using the above presented breviary, an SRM designed for light electric vehicle was obtained with the main dimensions which are depicted in **Figure 1**.

To certify that the machine meets the requirements of developing at 80 A, a torque of 3.4 Nm at 3400 rpm, in finite element analysis (FEA) model was created in Cedrat Flux 2D software. The current in the windings was handled using hysteresis controller referenced at 80 A as depicted in **Figure 2a**. At rated current the mean torque reaches the value of 3.4 Nm, but, despite attempts to reduce the torque ripple by design, these are still quite high. In such cases, the SRM cannot be used for electric propulsion systems as those ripples create high noise and vibration in the mechanical transmission and the car's body itself.

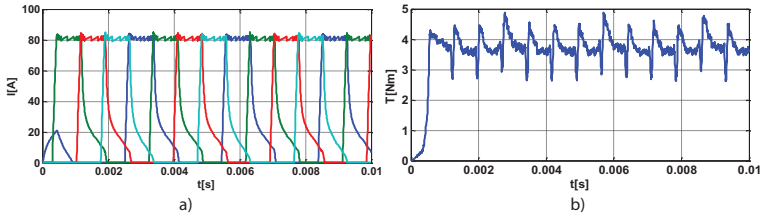


**Figure 2.** The simulation results of the designed SRM: (a) the phase currents and (b) the developed torque.

## 3. Torque linearization control strategies for the SRM

The results shown in **Figure 2** indicate that the operational skills of the SRM, but more, it is also proved that the torque ripples are too high compared to the requirements of an electric vehicle propulsion unit. The structure recorded a success up to an extent. However, the torque ripples need to be further reduce to fit the machine in the EV requirements. For this purpose, special control procedures are engaged, such as direct instantaneous torque control (DITC) [11, 12] or current profiling based on torque sharing functions (TSF) [13].

Before detailing each of the above-mentioned methods, some requirements regarding their implementation must be highlighted. Besides a good knowledge about the parameters of the machine, of the power converter and of the controller's sampling frequency, each of the two methods is based on inserting into the control model look-up-tables (LUT). For DITC, the LUT must contain information of the variation of the torque versus current and rotor position, as depicted in **Figure 3a**. Usually the content of this LUT is fetched from the FEA model of the machine. If the laboratory facility permits it, it is better to record this data from experimental measurements. However, as its name mentions it, DITC is an instantaneous torque control; hence, at each computation sample, the controller must have precise information of the torque values. This information can be extracted from the LUT, knowing precisely the shaft position and the measured phase current.

The second control strategy, the current profiling based on TSF, requires a reversed structure of the LUT depicted in **Figure 3a**, having the variation of the current versus torque and rotor

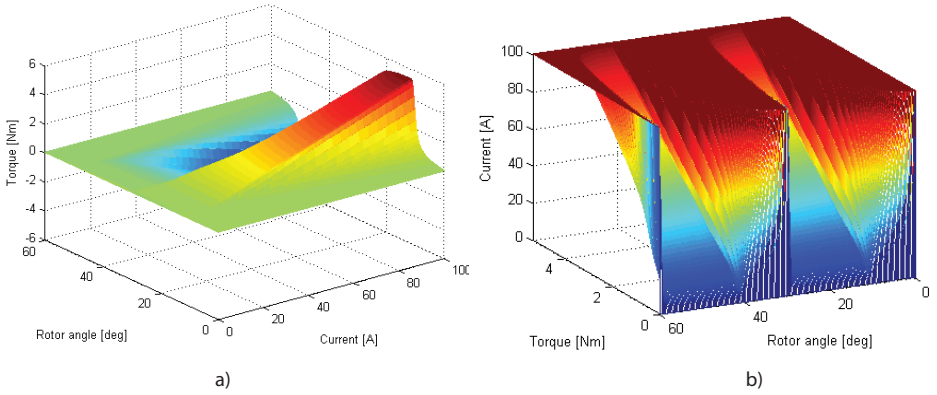


**Figure 3.** The look-up-table used for the DITC (a) and TSF (b).

position. The data can be obtained proceeding for a reversed interpolation of the torque versus current and rotor position, with respect to the phase current. This LUT is depicted in **Figure 3b**.

### 3.1. Direct instantaneous torque control (DITC)

The DITC (see **Figure 4a**) method [14] invokes a procedure of torque smoothening based on the control of instantaneous torque developed by the machine, using a hysteresis band. The main advantage of this procedure is that it does not require any PI (proportional integral) or PID (proportional integral derivate). The actual shape of the torque is regulated based on a double-layered hysteresis band. The comparison of the torque with the hysteresis band returns directly the gate signals for the power switches. As the torque is not measured directly from the machine, but it is estimated from the LUT, the setup does not require an instantaneous torque transducer which usually costs too much.

Practically, the DITC is implemented using two hysteresis bands, one larger than the other. The controller divides these into three regions, two of them form the torque reference to the upper and lower extremities and the main one is placed in the middle as depicted in **Figure 4a**.

During single phase conduction, the torque is regulated inside the limits of the main (inner) band (as shown in **Figure 4b**). In **Figure 4c**, with blue the voltage of the outgoing phase is depicted, while with red the voltage of the incoming one is represented. With the same colors, in **Figure 4d**, with blue the torque of the outgoing phase is represented while with red the torque of the incoming one is shown. The main involvement of the DITC is reflected during phase commutation. During phase commutation, the torque is regulated by the incoming phase, on one hand, to maintain it inside the inner hysteresis band, and on the other hand, by the outgoing one that becomes energized just enough to increase the torque when it falls and reaches the lower limit of the outer band. On increasing the torque, this will be re-established inside the inner band. At this point, the current increases close to maximum value, hence the torque tends to increase fast. To compensate this issue, the outgoing phase is again energized but with negative voltage (**Figure 4c**) to force fast-fall of the torque to maintain it in the desired

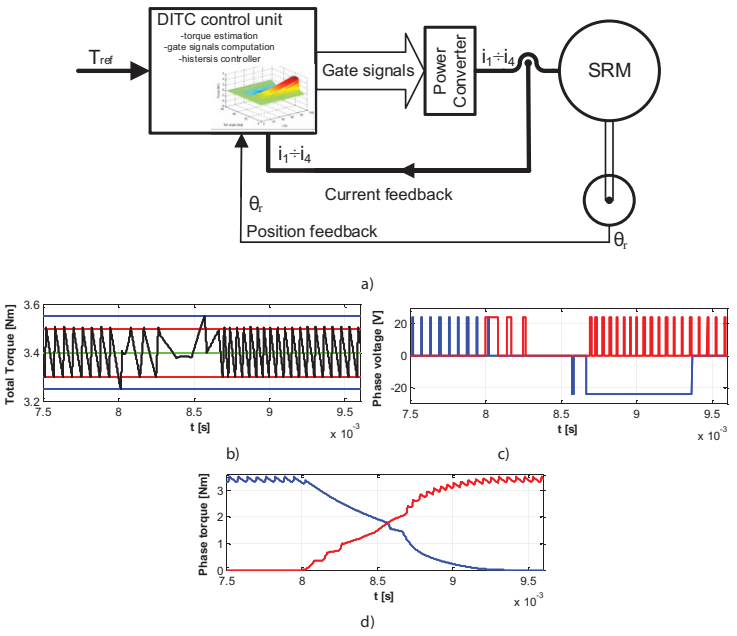


**Figure 4.** The DITC control scheme (a), the instantaneous torque (b), voltage of adjacent phases and (c) the phase torque (d).

band. From the moment when the incoming phase is energized, despite the times when the torque gets out of the inner hysteresis band, the outgoing phase is kept at zero voltage. Hence, the phase torque is regulated precisely during phase commutation, as seen in **Figure 4c**, time interval when usually the increased ripples appear.

### 3.2. Torque sharing functions (TSF)

Despite DITC, there are control methods that are more precise based on shaping the current and by this, automatically modifying the torque profile to become close to the linear one. The torque sharing function (TSF) is engaged mainly in the region of phase switching. The outgoing and incoming phase currents are profiled based on specific functions in order to compensate the ripples in the torque characteristic. One important issue that needs to be controlled for this strategy is the overlap angle [15] that needs to be precisely 15 mechanical degrees $\theta_{ov}$:

$$\theta_{ov} \leq \frac{\theta_{rot}}{2} - \theta_{off} \tag{28}$$

In Eq. (30), $\theta_{rot}$ denotes the period of the rotor and $\theta_{off}$ the turn off angle; with $\theta_{on}$ the turn on angle of the phase is denoted for all the following equations. A general rule for engaging the TSF of the rotor position described in Eq. (31) is valid for all the following analysed cases [16, 17]. As it can be seen there are five levels of the control based on the rotor position. While the machine phase is in non-conducting region, the TSF is null. During the increase and

decrease of the current, the slopes are described by functions $f_{inc}(\theta)$ and $f_{dec}(\theta)$. If the region of the phase is in full conduction (neither increase nor decrease of the current), the TSF becomes equal with the reference torque. As it can be seen that the profile of the current is obtained using the LUT data depicted in **Figure 3b**.

$$\mathrm{TSF}(\theta) = \begin{cases} 0 & 0 \le \theta \le \theta_{on} \\ f_{inc}(\theta) & \theta_{on} \le \theta \le \theta_{on} + \theta_{ov} \\ T_{ref} & \theta_{on} + \theta_{ov} \le \theta \le \theta_{off} \\ f_{dec}(\theta) & \theta_{off} \le \theta \le \theta_{off} + \theta_{ov} \\ 0 & \theta_{off} + \theta_{ov} \le \theta \le \theta_{p} \end{cases} \tag{29}$$

In total, there are four different types of TSF named after the mathematical operator that describes them: linear, sinusoidal, exponential and cubic.

The **linear TSF** refers to the fact that the instantaneous torque during phase commutation follows a linear variation with the rotor position. The function that describes this variation is detailed in Eq. (32) for the increasing and decreasing slopes.

$$\begin{aligned} f_{inc}(\theta) &= \frac{T_{ref}}{\theta_{ov}}(\theta - \theta_{on}) \\ f_{dec}(\theta) &= T_{ref} - \frac{T_{ref}}{\theta_{ov}}(\theta - \theta_{off}) \end{aligned} \tag{30}$$

It has to be noted that during phase commutation the incoming and outgoing phases of the machine are both active.

Using **sinusoidal TSF** implies using functions with sinusoidal or co-sinusoidal evolution of the TFS during phase commutation. The model that refers to such variations is detailed in Eq. (33).

$$\begin{aligned} f_{inc}(\theta) &= 0.5 \cdot T_{ref} - 0.5 \cdot T_{ref} \cos\left(\pi/\theta_{ov} \cdot (\theta - \theta_{on})\right) \\ f_{dec}(\theta) &= 0.5 \cdot T_{ref} + 0.5 \cdot T_{ref} \cos\left(\pi/\theta_{ov} \cdot (\theta - \theta_{off})\right) \end{aligned} \tag{31}$$

In Ref. [11], the functions detailed in Eq. (33) are presented only function of the on and off angles of the phase. Here, in order to improve the functionality, the overlap angle is also introduced.

The third model, the **exponential TSF**, considers the on and off angles, the actual rotor position and the overlap angle too, as detailed in Eq. (34).

$$\begin{aligned} f_{inc}(\theta) &= T_{ref}\left[1 - \exp\left(\frac{-(\theta - \theta_{on})^2}{\theta_{ov}}\right)\right] \\ f_{dec}(\theta) &= T_{ref}\left[\exp\left(\frac{-(\theta - \theta_{off})^2}{\theta_{ov}}\right)\right] \end{aligned} \tag{32}$$

**Cubic TSF** is the last involved method, described as third degree polynomial functions for both increasing and decreasing slopes, as explained in Eq. (35).

$$f_{\text{inc}}(\theta) = \frac{3T_{\text{ref}}}{\theta_{\text{ov}}^2}(\theta - \theta_{\text{on}})^2 - \frac{2T_{\text{ref}}}{\theta_{\text{ov}}^3}(\theta - \theta_{\text{on}})^3$$
$$f_{\text{dec}}(\theta) = T_{\text{ref}} - f_{\text{inc}}(\theta - \theta_{\text{off}} + \theta_{\text{on}}) \tag{33}$$

Plotting in **Figure 5**, all the four functions superimposed for comparison some important remarks can be underlined.

As depicted in **Figure 5a**, the TSF for the cubic and sinusoidal evolutions nearly overlap and for a better comparison in **Figure 5b**, a zoomed plot of the rising slopes of the functions is depicted.

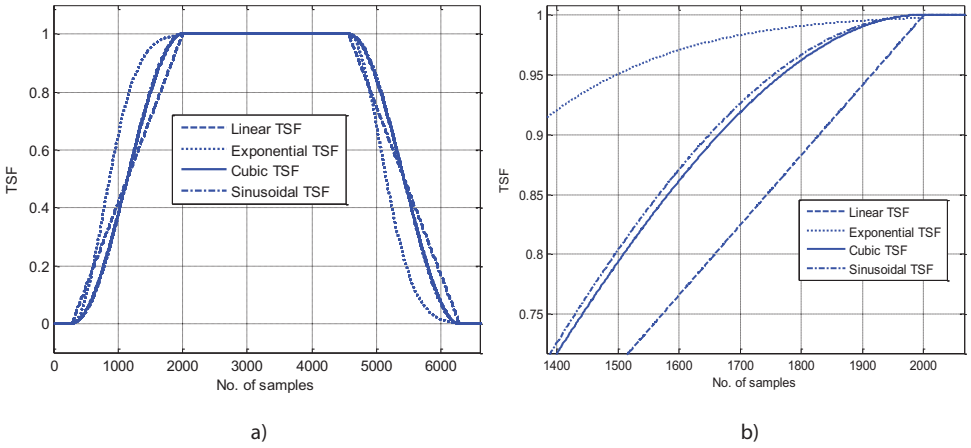


**Figure 5.** The variation of the TSFs used in the SRM controller.

The exponential one has the largest deviation from the linear one, the latter being considered for reference. Another important remark to be mentioned is that the machine's geometry or its parameters do not have an important significance over the effectiveness of the TSFs. Main modifications regard changing the stator to rotor pole ratio. However, it is possible to invoke optimization regarding the losses and the torque variation [17], together with the on and off switching angles.

### 3.3. Testing the control strategies for torque linearization

As already stated, and depicted in **Figure 2**, the torque ripples of the SRM with 'natural' hysteresis control strategy are too high to be used in EV propulsion systems [18]. However, applying the control procedures detailed in Section 3.2, this drawback can be compensated to reach a torque characteristic close to a linear one, comparable with the one of a permanent magnet synchronous or induction machine. To test the control strategies, a Matlab/Simulink model was created for the SRM based on a hybrid model based on equations and on data both fetched from the FEA model.

In **Figure 6a** and **b**, the simulation results for the DITC are depicted for an imposed speed of 1000 rpm testing at 1 and 3 Nm. The phase currents and the phase torques provide information of the contribution of each of them to the total electromechanical torque development. The latter, as seen, reaches a quite linear characteristic, which is maintained inside the hysteresis bands. One important mention that needs to be expressed is that for such simulation or real control, the computation step time must be imposed to values that allow at least 5–10 steps inside the hysteresis band. Another important issue is that the width of the bands automatically increases the switching frequency of the transistors. Hence, a compromise between the latter and the type of power switch used must be considered when sizing the bands.

Plotting the results for the linear TSF was accomplished in **Figure 6c** and **d** for the same conditions as for the DITC. There are similarities between them; however, the results for the linear TSF are smoother than those obtained with DITC. The variation of the phase torque during phase switching is quite linear, as expected for this method. Both for the DITC and the linear TSF tests were performed at low and rated torque to prove the operational skills in extreme conditions. As **Figure 6** shows that the expectations are reached in all the cases. Tests were performed ranging the rotor speed from low to rated one and still the controller responded well, linearizing the torque as expected.

The other three TSF strategies, the exponential, cubic and sinusoidal ones were tested for 1000 rpm at 3 Nm and are depicted in **Figure 7**. As seen, these too can linearize the shape of the instantaneous torque.

However, the lowest ripple is yelled by the exponential TSF while for the cubic and sinusoidal, during phase commutation there are some spikes that are visible in the plots. However, as

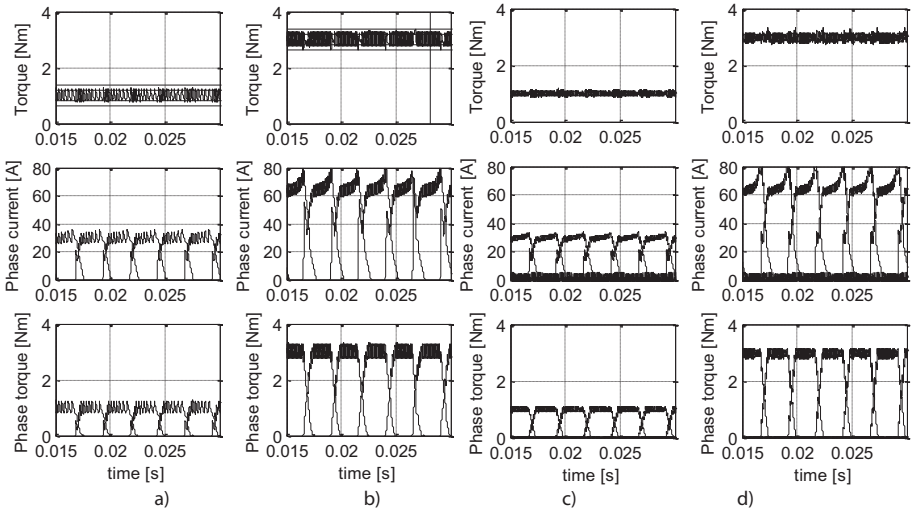


**Figure 6.** Simulated results for: (a) DITC @1 Nm, (b) DITC @ 3 Nm, (c) linear TSF @1 Nm and (d) linear TSF @3 Nm.

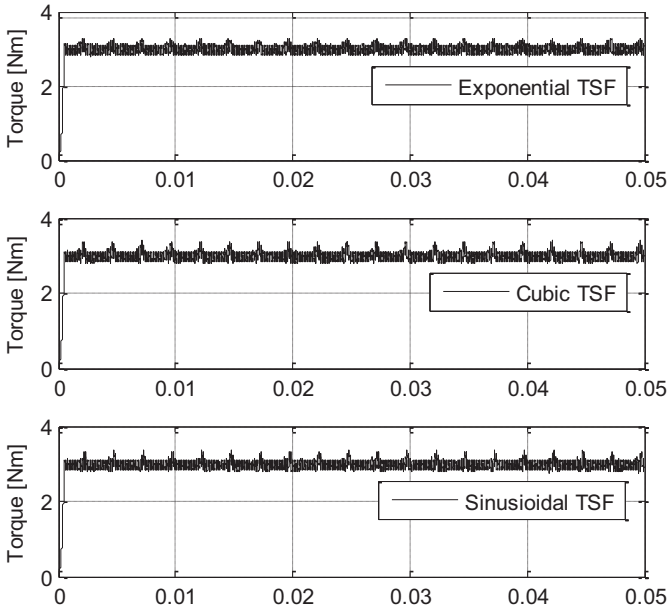


**Figure 7.** Simulated results for exponential, cubic and sinusoidal TSF @3 Nm.

global conclusion, the DITC and all the four TSFs can move the SRM from the point of high torque ripples to the point where these are neutralized by obtaining a linear characteristic. By this, the SRM becomes a candidate with serious advantages for the field of electric vehicle propulsion systems, combining low costs, high efficiency, fault tolerance and linear torque, over the entire range of speed and torque values.

## 4. Custom made SRM electronic converter architecture

In SRM-drive application, the 48 V input voltage seems to present some advantages in comparison with the 24 V systems. For application where the 48 V is not available, as for the designed SRM, this section is presenting a possible solution regarding the electronics that can enhance the performances of SRM in 24 V systems. One way to boost the input voltage by means of a front-end converter is increasing the voltage up to 48 V. For this, numerous electronic circuits can be implemented [19]. Usually, these converters are using an inductance that can increase the size of the converter, but also its price.

In this section, based on a derived C-dump topology [20], a low-cost SRM electronic circuit is presented which can add a boost voltage to a regular asymmetrical converter, increasing the overall performances of the drive system. The present circuit is fed from a 24-V power supply, as designed, and can perform in some situations like the classic SRM converter with 48 V input

voltage. This is achieved, as depicted in **Figure 8**, by adding the transistor Q and the capacitor C to a regular asymmetrical SRM drive. Moreover, the input diode D is needed for proper control of the power flow. This diode is adding some losses to the circuit, but the auxiliary feature obtained by adding protection in revered polarizations is an important characteristic for automotive electronics. The auxiliary circuit is boosting the voltage across the capacitor C, by recovering the energy from the motor during de-fluxing. The voltage across C can be higher than the input voltage and this energy can be re-used to drive the motor when needed. Thus, with proper control, the motor can be fed in this situation with a higher voltage then the input voltage. If the voltage across C is regulated to a 48 V, the drive can act in some working modes like a 48-V drive system.

The energy recovered from the motor is not high enough to fed the motor all the time, but if we consider that the high voltage is strongly needed only in some particularly situations like the beginning of the phase energizing, the stored energy in the capacitor C could be sufficient.

The circuit is presented in **Figure 8**, while **Figure 9** highlights the main working modes for one phase. In the first two figures (**Figure 9a** and **b**), the phase fluxing is presented, while **Figure 9c** and **d** highlights de-fluxing possible working modes.

In the followings, two comparison situations will be presented to highlight the advantages obtained by using the presented topology in correlation with the regular asymmetrical SRM converter, applied on a 48-V SRM. In **Figure 10** and **11**, the instantaneous toque, the phase current and the phase voltage are presented at 800 and 1000 rpm, for the analyzed converter topologies.

This circuit is working with different voltage levels, thus the control of the T1 switch should be correlated with the working speed. At low speed, the energy needed to obtained the 48 V across the C is easily obtained, thus the excess energy is used during normal phase operation, or correlated with special control algorithms that can be used for smoothing the torque ripple at low speeds. At high speeds, the energy recovered in the capacitor C is just high enough for full or partial first energising of the phase coil.

If the energy recovered in the capacitor C is managed in the right way, the drive converter can act almost like a 48-V converter. This is boosting the performance of the drive system, by

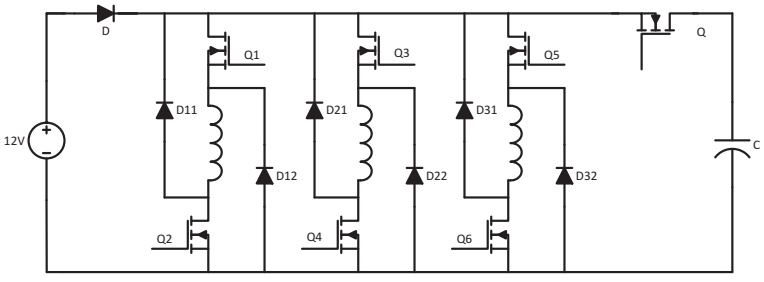


**Figure 8.** Proposed SRM boost converter.

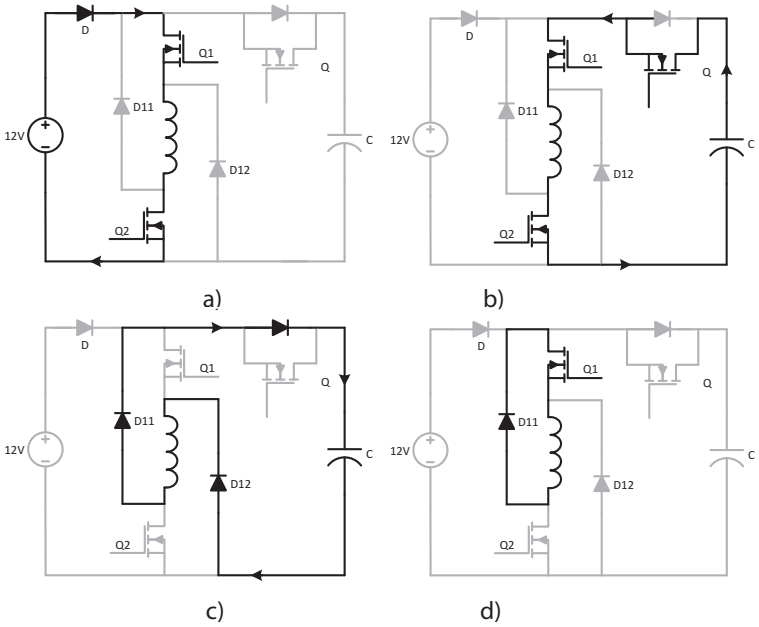


**Figure 9.** Operation points for the investigated converter topology; one phase is considered; (a and b) phase energising; (c and d) phase de-fluxing.

adding flexibility regarding the torque control, extend the working range and is expected to add 3–5% on the system efficiency. Moreover, the presented converter topology can be used to enhance the performances also in 12 V systems.

Comparing the results in **Figure 10** and **11**, a first remark regards the slope of the energized coil. It can be observed that due to boosted voltage, the slope of the current is faster than in the

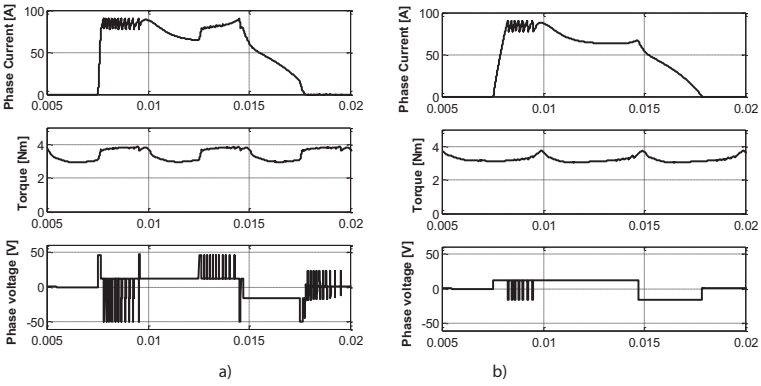


**Figure 10.** Waveforms for the proposed converter (a) and regular asymmetrical SRM converter (b) at 1000 rpm.

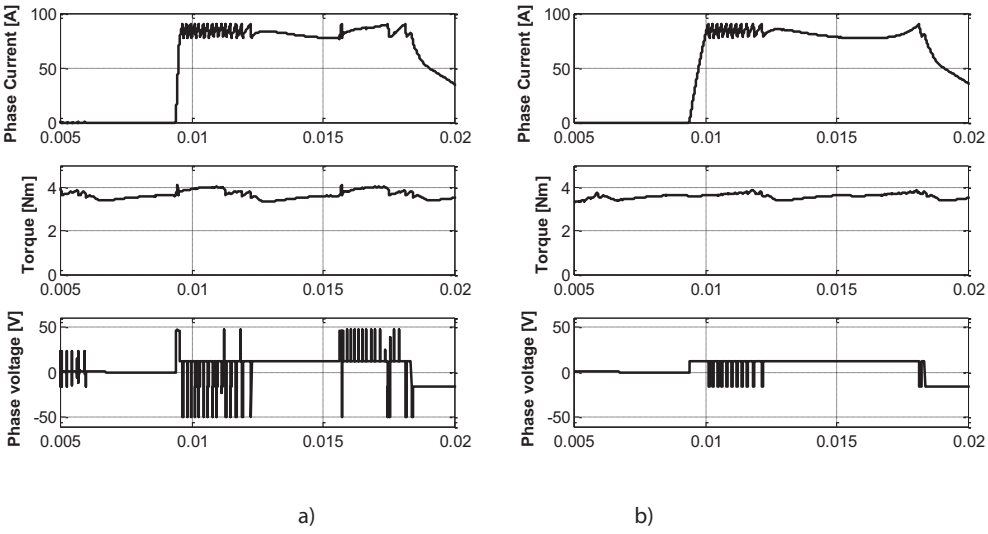


**Figure 11.** Waveforms for the proposed converter (a) and regular asymmetrical SRM converter (b) at 800 rpm.

case of non-boosted one. On the other hand, if comparing the mean torque, developed by the machine for all cases, at 1000 rpm this value reaches 3.36 Nm for the boosted case, instead of 3.18 Nm for the regular converter. For the second case of analysis, the mean torque in the case of the modified converter yells for 3.65 Nm while for the regular one reaches only 3.55 Nm.

Implying such changes, one can express that with low cost modifications of a classical asymmetrical converter structure, higher performances can be obtained. It is true that the gain is not extremely high, but considering that the subject is dedicated to electric propulsion systems, each step forward in increasing the autonomy of the vehicle is an addition to the actual progress of science in this field of high interest nowadays.

## 5. Conclusions

The goal of the chapter is to offer a solution as a complete development tool for the reader to be able to design an SRM, design an increased performance power converter for it and create smart control strategies to reach linear torque characteristics as requirement for electric propulsions. Combining analytical models of the design with finite element analysis-based validation can reach in a properly design machine. Usually, a backtracking concept is engaged, performing changes at the level of design and observe performance modifications during FEA simulations. Once the machine fits in the designer's expectations, adding an electronic power converter and torque smoothening strategies becomes the second and third steps in the design of the system.

The issues detailed in the chapter points out that an SRM can be used easily in the field of electric propulsion. Placing it in the list of serious candidates for the automotive industry, adds to the

actual status of research focused on PMSMs or AC machines, with a low cost, robust and simple solution. Comparing the SRM with the above-mentioned machines, it can be stated that all need precise rotor position measurement, performed by a resolver, all need power electronics and a main electronic digital controller. However, the price of electronics nowadays decreased a lot due to fast advance. Hence, the battle on financial level is now dictated by the architecture of the machine, the materials used and the complexity of its geometry. Regarding the magnetic cores, the windings, the use of permanent magnets, etc., a comparative analysis of the ac machines with the SRM points strongly for higher costs and more complex manufacturing process.

Worldwide, there are already several companies that invest in development of SR machines for propulsion systems, both for light and heavy electrical vehicles.

## Author details

Mircea Ruba* and Petre Dorel Teodosescu

*Address all correspondence to: mircea.ruba@emd.utcluj.ro

Technical University of Cluj Napoca, Cluj, Romania

## References

[1] Vrazic M, Vuljaj D, Pavasovic A, Paukovic H. Study of a vehicle conversion from internal combustion engine to electric drive. In: IEEE International Energy Conference, Croatia; 13-16 May 2014. pp. 1544–1548. ISBN: 978-1-4799-2449-3

[2] Ruba M, Viorel IA, Szabó L. Modular stator switched reluctance motor for fault tolerant drive systems. IET Electric Power Applications. 2013;**7**(3):159–169. ISSN: 1751-8660

[3] Raminosoa T, Blunier B, Fodorean D, Miraoui A. Design and optimisation of a switched reluctance motor driving a compressor for a PEM Fuel cell system for automotive applications. IEEE Transactions on Industrial Electronics. 2010;vol.9, pp:2988–2997. ISSN 0278-0046

[4] Chindriş V, Ruba M, Fodorean D. Design and testing a low-voltage high-current drive for SRMs used in light electric vehicles. In: Power Electronics and Motion Control Conference and Exposition (PEMC); 16th International; 21-24 September 2014. 2014. pp. 137–142. ISSN: 978-1-4799-2060-0

[5] Radun A. Design considerations for the switched reluctance motor. Proceedings of IEEE Transactions on Industrial Applications. 1995;**31**(5):1079–1087. ISSN: 0093-9994, DOI: 10.1109/28.464522

[6] Krishnan R. Switched Reluctance Motor Drives – Modeling, Simulation, Analysis, Design, and Applications. Industrial Electronics Series, publisher: CRC Press; 2001

[7] Radun A. Analytically computing the flux linked by a switched reluctance motor phase when the stator and rotor overlap. Proceedings of IEEE Transactions on Magnetics. 2000;**36** (4):1996–2003, ISSN: 0018-9464

[8] Huang S, Luo J, Leonardi F, Lipo T. A general approach to sizing and power density equations for comparison of electrical machines. IEEE Transactions on Industry Applications. 1998;**34**(1):92–97. ISSN: 0197-2618

[9] Szabó L, Ruba M. Using Co simulations in fault tolerant Machine's study. In: Proceedings of the 23rd European Conference on Modelling and Simulation (ECMS '2009); Madrid (Spain); 2009. pp. 756–762. ISBN: 978-0-9553018-8-9

[10] Raulin V, Radun A, Husain I. Modelling of losses in switched reluctance machines. Proceedings of IEEE Transactions on Industrial Applications. 2004;**40**(6):1560–1569. ISSN: 0093-9994

[11] Petrus V, Pop AC, Martis CS, Iancu V, Gyselinck J. Direct instantaneous torque control of SRMs versus current profiling—Comparison regarding torque ripple and copper losses. In: 13th International Conference on Optimization of Electrical and Electronic Equipment (OPTIM); 24-26 May 2012. pp. 366–372. ISSN: 1842-0133

[12] Inderka RB, De Doncker RW. DITC-Direct instantaneous torque control of switched reluctance drives. In: 37th Annual Meeting IEEE IAS Conference. 2002;**39**(4):1046–4051. ISSN: 0093-9994

[13] Ruba M, Fodorean D. Development of a complete motor-drive solution for light EV based on a SRM. In: 2016 International Conference and Exposition on Electrical and Power Engineering (EPE), Iasi, Romania. pp. 197–204, ISBN: 978-1-5090-6129-7

[14] Fuengwarodsakul NH, De Doncker RW. Instantaneous torque controller for switched reluctance vehicle propulsion drives. In: 20th Electric Vehicle Symposium; November 15-19, 2003 Long Beach, California

[15] Sahoo NC, Xu JX, Panda SK. Low torque ripple control of switched reluctance motors using iterative learning. IEEE Transactions Energy Conversion. 2001;**16**(4):318–326. ISSN: 0885-8969

[16] Lee DH, Liang J, Lee ZG, Ahn JW. A simple nonlinear logical torque sharing function for low-torque ripple SR drive. IEEE Transactions on Industrial Electronics. 2009;**56**(8):3021–3028. ISSN: 0278-0046

[17] Mademlis C, Kioskeridis I. Performance optimization in switched reluctance motor drives with online commutation angle control. IEEE Transactions on Energy Conversion. 2003;**18**(3):448–457

[18] Ruba M, Fodorean D. Motor-drive solution for light electric vehicles based on a switched reluctance machine. In: 2016 IEEE International Conference on Automation, Quality and Testing, Robotics, AQTR; 19th-21st May 2016; Cluj Napoca, Romania. ISBN: 978-1-4673-8691-3

[19] Tomaszuk A, Krupa A. High efficiency high step-up DC/DC Converters a Review. Bulletin of the Polish Academy of Sciences Technical Sciences. 2011;**59**(4):475–483. ISSN: 2300-1917

[20] Lee TW, Yoon YH, Yuen-Chung Kim, Lee BK, Won CY. Control of c-dump converters fed switched reluctance motor on an automotive application. Electric Power Systems Research. 2007;**77**(7):804–812. ISSN 0378-7796